PERGAMON

International Journal of Heat and Mass Transfer 44 (2001) 953–965

International Journal of HEAT and MASS TRANSFER

www.elsevier.com/locate/ijhmt

Fluid flow, heat transfer and solidification in the mold of continuous casters during ladle change

X.K. Lan [1], J.M. Khodadadi *

Department of Mechanical Engineering, Auburn University, 201 Ross Hall, Auburn, AL 36849-5341, USA

Received 2 July 1999; received in revised form 17 April 2000

Abstract

A computational study of the transient two-dimensional turbulent fluid flow, heat transfer and solidification in continuous casting molds during the ladle change operation is presented. The computations are based on an iterative, finite-volume numerical procedure using primitive dependent variables, whereby the governing time-dependent continuity, momentum and energy equations in combination with a low-Reynolds number turbulence model are solved. A single-domain enthalpy formulation is used for simulation of the phase change phenomenon. The effect of phase change on convection is accounted for using a Darcy's law-type porous media treatment. It is shown that due to the time-dependence of the inlet temperature during the ladle change, the volume occupied by the liquid phase generally expands in the radial direction during each cycle, whereas the axial extent of the liquid pool shrinks due to the greater influence of the buoyancy force. The increase in size for the liquid pool depends on the casting speed and is as much as 25% when compared to the steady-state value. The size of the mushy zone does not vary greatly over the period of ladle change. The thickness of the solidified shell shrinks during the ladle change operation to some extent. Casting surface temperatures vary over the two cycles of the ladle change operation and distinct temperature rise signatures were detected.

1. Introduction

In recent years, the continuous casting process in which molten metal is constantly cast into semi-finished shapes has been widely adopted in the steel and non-ferrous metal producing industry, mainly due to its economic advantages associated with increased yields and the elimination of intermediate processing steps. The mold is one of the most important components of a continuous caster (Fig. 1). It is known that the quality of metal castings is affected by a number of parameters directly related to the turbulent transport processes taking place within the mold. An understanding of transport processes in the liquid metal pool is of particular importance because it can be used in controlling the growth rate of the solidifying shell, thus affecting the microstructure of the final casting. The transport processes also control the formation of various defects, which can hamper subsequent processing. Examples of defects formed in this region are macro-segregation, surface irregularities, such as cold folding and oscillation marks, and more serious defects such as longitudinal or transverse cracks. A more catastrophic problem, which may occur, is ''breakout'', where the shell ruptures and molten metal is discharged in an uncontrolled manner.

2. Review of literature

Previous research in the area of continuous casting has covered both mathematical modeling of fluid flow and heat transfer, and experimental studies involving the use of water models. Szekely and Yadoya [1]

* Corresponding author. Tel.: +1-334-844-3333; fax: +1-334-844-3307.

E-mail address: jkhodada@eng.auburn.edu (J.M. Khodadadi).

[1] Present address: Beloit Corporation, 1165 Prairie Hill Road, Rockton, IL 61072-1595.

0017-9310/01/$ - see front matter
PII: S0017-9310(00)00145-9

Nomenclature

A	porosity function, kg/s m^3
c_p	specific heat, J/kg K
C_0	Darcy coefficient, kg/s m^3
d_j	jet diameter, m
Fr	Froude number, defined as $U_j^2/g(2R)$
g	gravitational acceleration, m/s^2
Gr	Grashof number, defined as $g\beta(2R)^3(T_{ref}-T_s)/\nu^2$
h_1, h_2	heat transfer coefficients of the mold and spray, respectively, W/m^2 K
k	turbulence kinetic energy, m^2/s^2
P	pressure, Pa
Pr	Prandtl number, defined as $\mu c_p/\kappa$
r	radial coordinate, m
r_j	radius of the jet, m
R	radius of the mold, m
R_t	turbulence Reynolds number, defined as $k^2/\nu\varepsilon$
R_y	turbulence Reynolds number, defined as $(R-r)k^{1/2}/\nu$
Re_j	Reynolds number of the jet, defined as $U_j d_j/\nu$
t	time, s
T	temperature, K
T_a	ambient temperature, K
T_j	jet's exit temperature, K
T_{ref}	reference temperature, defined as jet's exit temperature under steady-state conditions, K
T_w	temperature of the surface of casting, K
U	time-averaged axial velocity, m/s
U_c	casting speed, m/s
U_j	jet's uniform exit velocity, m/s
V	time-averaged radial velocity, m/s
z	axial coordinate, m

Greek symbols

β	thermal expansion coefficient, K^{-1}
ε	rate of dissipation of turbulence energy, m^2/s^3
κ	thermal conductivity, W/m K
μ	dynamic viscosity of the fluid, Ns/m^2
ν	kinematic viscosity of the fluid, m^2/s
ρ	density of the fluid, kg/m^3

Subscripts

j	related to the jet
t	turbulent

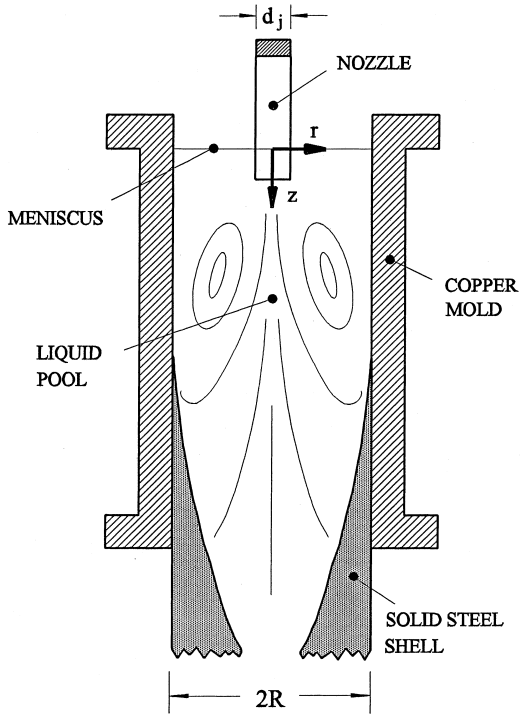

Fig. 1. Molten metal flow inside the mold.

investigated the flow field in the mold region of continuous casting systems experimentally, by performing flow visualization and velocity measurements in a water model. Both straight-through and radial flow nozzles were used in their experiments. Water was pumped at rates corresponding to casting speeds of 76.2–127 cm/min (30–50 in./min). Impact tubes in combination with wall static pressure readings were used to obtain velocity profiles. The existence of a turbulent recirculatory motion driven by the incoming fluid stream in the upper part was verified. The penetration length of the separated zone in the system approached 4–6 mold diameters for the straight-through nozzle. Szekely and Yadoya [2] later gave the theoretical description of the velocity and temperature fields in the mold region, by solving appropriate turbulent flow equations. The vorticity–stream function approach combined with a one-equation turbulence model (transport for k plus a given length-scale) was used for prediction of the time-averaged features of the flow and thermal fields. Jezek [3] studied the penetration depth of the jet issuing from a straight-through nozzle and the strength of separated flow in a water model. In this flow visualization experiment, tufts were used to determine the mean value of the length of the recirculation zone. Khodadadi et al. [4] have reported results of flow visualization studies (tuft grid, dye tracer and hydrogen bubble techniques) in an aqueous system using both straight-through and radial-entry nozzles.

With the greater availability of powerful computational hardware and development of sophisticated computational codes, realistic processing conditions and simulations of the transport processes within the mold

have been reported in recent years [5–7]. The coupled turbulent flow and heat transfer equations accounting for buoyancy, surface tension and phase change were solved by Shyy et al. [5] in order to simulate the titanium alloy continuous ingot casting in an electron beam melting process. A Darcy's law type of porous media treatment was utilized to account for the effect of phase change on convection. A modified version of a low-Reynolds number turbulence model was used and an adaptive grid solution method was utilized. Simulations were carried out for processing under standard gravity and microgravity conditions. The results were compared with an experimentally determined pool profile from a casting ingot. Shyy et al. [6] later extended their previous work [5] to study the effect of correlation fluctuations between velocity and temperature, in addition to correlated fluctuations between velocity and release of latent heat on temperature contours and phase change. Coupled turbulent flow, heat and solute transport in the mold of a continuous billet caster was studied numerically for steady-state operating conditions by Aboutalebi et al. [7]. Using a low-Reynolds number turbulence model and a continuum model for treatment of various phases, they studied the effects of the casting speed, steel grade, nozzle configuration on the flow field, solidification pattern and carbon segregation for a binary Fe–C alloy system. The trajectory of inclusions and their density distributions were calculated and reasonable agreements with measurements were reported.

In the present paper, a computational study of the transient two-dimensional turbulent fluid flow, heat transfer and solidification in a round steel bloom caster fed by a straight-through entry nozzle is presented. The time dependence of the flow field, temperature contours and solidification patterns are due to a ladle change operation. The study is motivated by the recent findings of Chakraborty and Sahai [8] who investigated the effect of varying ladle stream temperature on fluid flow and heat transfer in a two-strand slab caster tundish with weirs and dams, by solving the transient 3-dimensional transport equations. The ladle temperature was allowed to decrease uniformly by 25°C over a period of 50 min. During the first half of teeming, the incoming melt becomes cooler than the melt temperature in the bulk of the tundish. Consequently, an inverse flow pattern develops, which continues for the remaining half of the teeming period, which can lead to higher inclusion content of the castings. Greater industrial attention to quality improvement associated with unsteady-state slab portions, which mainly correspond to ladle changes, has revealed that the tundish exit temperature (same as the mold inlet temperature in this paper) varies over the period of teeming. The effect of this time-dependent inlet temperature variation due to ladle change on the transport processes in the mold is investigated in this paper.

3. Computational technique

The computational results presented in this paper were obtained by utilizing the SIMPLE procedure of Patankar [9]. The elliptic time-averaged transport equations governing this time-dependent axisymmetric problem are of the general form

$$\frac{\partial(\rho\phi)}{\partial t} + \nabla \cdot (\rho \mathbf{V}\phi) = \nabla \cdot (\Gamma_\phi \nabla\phi) + S^\phi, \tag{1}$$

where $\mathbf{V}$ is the velocity vector with its two components U and V representing the time-averaged velocities in the axial (z)- and radial (r)-directions, respectively. Due to the axisymmetric nature of the problem, tangential gradients vanish. The variable ϕ represents various time-averaged quantities, i.e., mean velocities, enthalpy, turbulence kinetic energy and turbulence energy dissipation rate. The quantities Γ_ϕ and S^ϕ represent the diffusivity of the transported variable ϕ and the source term for various transport equations, respectively. The appropriate transport equations are summarized in Table 1.

3.1. Turbulence model

The low-Reynolds number k–ε turbulence model of Lam and Bremhorst [10] in combination with the suggested turbulence energy dissipation rate boundary condition of Patel et al. [11] were utilized for the present computations. Very recently, the experimental and computational work of Lan et al. [12] showed that among five variations of low-Reynolds number k–ε turbulence models, the Lam and Bremhorst model performs very well in predicting the velocity and turbulence fields in submerged jets which involve complex reverse flow and are directly relevant to the flow in continuous casting molds. The details of this turbulence model are summarized in Table 2.

3.2. Phase change model

The *enthalpy formulation* which is used in this study belongs to the single-region (or continuum) class of methods. The present form of the source term for the thermal energy equation in Table 1 can be derived by splitting the total enthalpy of the material into the sensible enthalpy ($h = c_p T$) and the latent heat (H) [13,14]. A linear relationship between the latent heat and temperature is used, i.e.,

$$H = f_l H_f, \tag{2}$$

where H_f is the latent heat of the phase change and the liquid fraction (f_l) is given by

Table 1
Transport equations[a]

Equations	Variables		
	ϕ	Γ_ϕ	S^ϕ
Continuity	1	0	0
Axial momentum	U	μ_{eff}	$\frac{\partial}{\partial z}\left(\mu_{\text{eff}}\frac{\partial U}{\partial z}\right)+\frac{1}{r}\frac{\partial}{\partial r}\left(r\mu_{\text{eff}}\frac{\partial V}{\partial z}\right)-\frac{\partial P}{\partial z}+\rho g\beta(T_{\text{ref}}-T)+A(U-U_{\text{c}})$
Radial momentum	V	μ_{eff}	$\frac{\partial}{\partial z}\left(\mu_{\text{eff}}\frac{\partial U}{\partial r}\right)+\frac{1}{r}\frac{\partial}{\partial r}\left(r\mu_{\text{eff}}\frac{\partial V}{\partial r}\right)-\frac{\partial P}{\partial r}-2\mu_{\text{eff}}\frac{V}{r^2}+AV$
Thermal energy	h	$\frac{\mu}{Pr}+\frac{\mu_{\text{t}}}{Pr_{\text{t}}}$	$G-\frac{\partial(\rho H)}{\partial t}-\nabla\cdot(\rho \boldsymbol{V}H)-\nabla\cdot(\rho(\boldsymbol{V}-\boldsymbol{V}_{\text{c}})(H_f-H))$
Turbulence kinetic energy	k	$\mu+\frac{\mu_{\text{t}}}{\sigma_k}$	$G-\rho\varepsilon-\rho D$
Turbulence dissipation rate	ε	$\mu+\frac{\mu_{\text{t}}}{\sigma_\varepsilon}$	$\frac{\varepsilon}{k}(C_1 f_1 G-C_2 f_2\rho\varepsilon)+\rho E$

[a] *Notes:*

$$G=\mu_{\text{t}}\left\{2\left[\left(\frac{\partial U}{\partial z}\right)^2+\left(\frac{\partial V}{\partial r}\right)^2+\left(\frac{V}{r}\right)^2\right]+\left(\frac{\partial U}{\partial r}+\frac{\partial V}{\partial z}\right)^2\right\}=\text{turbulence generation.}$$

$\boldsymbol{V}_{\text{c}}$ is the casting speed vector.
$\mu_{\text{eff}}=\mu+\mu_{\text{t}}$.
μ = dynamic viscosity of the fluid.
$\mu_{\text{t}}=\rho C_\mu f_\mu\frac{k^2}{\varepsilon}$ = turbulent viscosity.
σ_k and σ_ε are effective Prandtl numbers.
$A=\frac{-C_0(1-f_l)^2}{f_l^3}$.
$Pr_{\text{t}}=1.0$.
For values of $C_\mu, C_1, C_2, f_1, f_2, f_\mu, \sigma_k, \sigma_\varepsilon$, D and E, see Table 2.

$$f_l=\begin{cases}1 & T>T_l,\\ \frac{T-T_{\text{s}}}{T_l-T_{\text{s}}} & T_{\text{s}}\leqslant T\leqslant T_l,\\ 0 & T<T_{\text{s}},\end{cases}\tag{3}$$

where T_l and T_{s} are the liquidus and solidus temperatures, respectively.

3.3. Effect of phase change on convection and turbulence model

A Darcy's law-type of porous medium treatment [13] is utilized to account for the effect of phase change on convection. In Table 1, $A(U-U_{\text{c}})$ and AV are the Darcy damping terms for the axial and radial momentum equations, respectively. In order to account for the phase change in the turbulence model, the damping function f_μ in the turbulence model (Table 2) is multiplied by $\sqrt{f_l}$ as suggested by Shyy et al. [5].

3.4. Boundary conditions

The boundary conditions utilized were those of the standard practice in numerical computations. At the outlet station, which was placed 25 mold radii downstream of the inlet plane, the flow was assumed to be fully developed. The radial component of velocity and the normal gradients of other variables were set to zero at the symmetry axis. Fine grids were placed next to casting surface and with the use of a low-Reynolds number turbulence model, the computations were extended to the surface. On the casting surface next to the mold, the radial velocity component and the turbulence kinetic energy were set to zero. The axial velocity component on the casting surface next to the mold was set according to the following relations:

Table 2
Turbulence model constants and terms [10,11]

$C_\mu=0.09$	$C_1=1.44$	$C_2=1.92$	
$\sigma_k=1.0$	$\sigma_\varepsilon=1.3$	$D=0$	$E=0$
$f_1=1+\left(\frac{0.05}{f_\mu}\right)^3$		$f_2=1-\mathrm{e}^{-R_{\text{t}}^2}$	
$f_\mu=\left(1+\frac{20.5}{R_{\text{t}}}\right)[1-\exp(-0.0165R_y)]^2$			
$\frac{\partial\varepsilon}{\partial y}=0$ at the wall $(r=R)$			

$$U_{r=R} = 0 \quad \text{for } T_s < T_{r=R}, \tag{4}$$

$$U_{r=R} = U_c \quad \text{for } T_{r=R} \leqslant T_s. \tag{5}$$

The gradient of the turbulence kinetic energy dissipation rate on the casting surface next to the mold was set to zero as suggested by Patel et al. [11] for the Lam and Bremhorst [10] low-Reynolds number model. The boundary conditions used for the energy equation at the casting-mold and casting spray interfaces were

$$-\kappa \left.\frac{\partial T}{\partial r}\right|_{r=R} = h_1\ (T_{r=R} - T_a) \quad \text{for } z \leqslant L, \tag{6}$$

$$-\kappa \left.\frac{\partial T}{\partial r}\right|_{r=R} = h_2\ (T_{r=R} - T_a) \quad \text{for } z > L, \tag{7}$$

where L is the length of the mold. The values of the heat transfer coefficients of the mold and spray (h_1 and h_2) were adopted from Ref. [15]. It is common practice in continuous casting literature to only identify the casting speed (U_c), which refers to the speed of the solidified bloom or slab far downstream. Using two casting speeds of 76.2 and 120 cm/min (30 and 47.24 in./min) in combination with the continuity equation (mold to jet diameter ratio of 8), the appropriate uniform values for the jet's axial velocity component (U_j) were assigned. The corresponding jet Reynolds numbers, $Re_j = U_j d_j/\nu$ were equal to 24,194 and 38,100. The Froude numbers based on the velocity of the jet and the mold diameter were 0.33 and 0.82. The Grashof number under steady-state operating conditions was 6.775×10^9. For the problem at hand which is a *mixed convection* problem, the ratio of $Gr/(Re_j)^2$ determines the importance of buoyancy-driven convection. The values of this ratio were 11.57 and 4.65 for the low and high casting speeds, respectively, which means that buoyancy-driven convection within the mold cannot be ignored. At the inlet plane, the radial component of the jet velocity was set to zero. In the absence of turbulence measurements, uniform values for turbulence kinetic energy and its dissipation rate at the jet exit were assigned according to

$$k_j = 1.5(0.026U_j)^2, \tag{8}$$

$$\varepsilon_j = C_\mu^{3/4} k_j^{1.5}/(0.09 r_j). \tag{9}$$

The geometrical parameters and operating conditions of the caster are summarized in Table 3. Specifically, the value of the Darcy coefficient was adopted in concert with the work of Aboutalebi et al. [7], who further discuss the choice of this controversial coefficient. The properties of molten steel were taken to be constant and are summarized in Table 4. The jet temperature was varied with time according to the results of Chakraborty and Sahai [8], which is shown in Fig. 2. Under steady-state conditions, the jet temperature was 1530°C (30° of superheat). At the beginning of the first cycle, the

Table 3
Operating conditions of the caster

Mold diameter ($2R$)	0.2032 m
Jet diameter (d_j)	0.0254 m
Mold length (L)	0.6 m
Casting speed (U_c)	0.0127 & 0.02 m/s
Jet speed ($U_j = (R/r_j)^2 U_c$)	0.8128 & 1.28 m/s
Darcy coefficient (C_0)	1.016×10^6 kg/s m^3
Jet's uniform exit temperature at steady-state (T_{ref})	1530°C
Ambient temperature (T_a)	30°C
Heat transfer coefficient for $z \leqslant 0.6$ m (h_1)	1163 W/m^2 K
Heat transfer coefficient for $z > 0.6$ m (h_2)	1395.6 W/m^2 K

Table 4
Thermophysical properties of steel

Density of molten steel (ρ)	7.5×10^3 kg/m^3
Viscosity of molten steel (μ)	6.4×10^{-3} Ns/m^2
Specific heat (c_p)	753.624 J/kg K
Thermal conductivity (κ)	35 W/m K
Latent heat of phase change (H_f)	2.7214×10^5 J/kg
Liquidus temperature (T_l)	1500°C
Solidus temperature (T_s)	1470°C
Thermal expansion coefficient (β)	10^{-3} K^{-1}

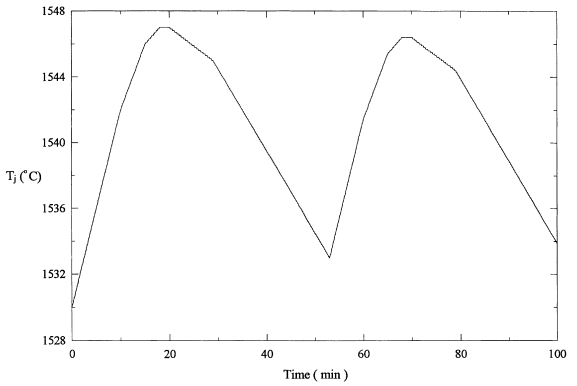

Fig. 2. Variation of the inlet mold temperature with time [8].

temperature ramps to 1547°C over a period of 18 min, after which it drops down to about 1533°C at the beginning of the second 50 min teeming cycle. The second cycle is very similar to the first one. In order to avoid complications associated with unsteady free surface motion and in view of the widespread use of flux powders on top of the meniscus in the industry, the meniscus was modeled to be fixed at $z = 0$. The axial velocity and the tangential derivative of the radial velocity were set to zero at the meniscus. In addition, the normal derivatives of k, ε and temperature vanish at the meniscus.

3.5. Initial conditions

The steady-state formulations of the governing equations were first utilized to calculate the steady-state field values for all the variables. The steady-state solution was then used as the initial conditions for the transient simulations.

3.6. Details of the numerical scheme

A 32×60 grid system was found to be sufficient to resolve the details of the flow and temperature fields based on comparison of the streamline contours and liquid–solid interface positions for various grid densities under steady operating conditions. Thirty-two expanding grids (i.e., the ratio of the lengths of the successive grids is equal to a specified constant greater than one) were employed in the streamwise direction. The radial grid layout was chosen to accommodate the presence of the shear layer and near-wall gradients. Accordingly, shrinking grids (same as expanding grids, but the constant is less than one) were employed from the symmetry axis to $r = r_j$. Expanding grids were then used from $r = r_j$ to $r = 0.45R$. Finally, shrinking grids were laid from $r = 0.45R$ to the casting surface. Staggered control volumes were used for the axial and radial velocity components. All other quantities of interest were computed at the grid points. The finite-volume form of the time-averaged transport equations was obtained by adopting a semi-integral approach to discretize the equations over each control volume of the computational grid, using a hybrid-difference scheme. The line-by-line method was used to obtain converged solutions iteratively, whereas relaxation factors were employed to promote stability of the process. For the low casting speed case under steady-state conditions, these parameters were 0.2, 0.2, 0.1, 0.15, 0.1 and 0.3 for U, V, T, k, ε and μ_t, respectively. The liquid fraction field was also underrelaxed with a value of 0.05, whereas no relaxation was applied to the pressure correction field. The converged results of the low casting speed case were used as the initial field for the high casting speed steady-state run. Thus, less stringent underrelaxation factors were used without the risk of divergence. These were 0.5, 0.45, 0.5, 0.5, 0.45, 0.3 and 0.45 for U, V, T, k, ε, μ_t and f_l, respectively. During the steady-state runs, the iterations were terminated when all the absolute residuals (normalized by the corresponding inlet plane fluxes) were less than 10^{-6}. The number of iterations needed to achieve the converged solution fields were 67,889 and 18,982 for the low and high casting speed cases, respectively. The temporal derivatives were treated using an implicit formulation, which demands no stability requirement. The time step used for the transient calculations was 4 s, whose predictions were found to be similar to the results based on a shorter time step of 1 s. During all the transient computations, the underrelaxation parameters corresponding to the high casting steady-state case discussed above were used and the convergence criterion was relaxed to 10^{-5}. The transient calculations were carried out for 100 min simulating two successive heats of 50 min duration each (Fig. 2). Typically, it took about 2000–2500 iterations to converge for each time step. The CPU times per iteration were 0.104 and 0.107 s for the steady-state and transient computations, respectively, regardless of the casting speed. Total CPU time corresponding to the simulation of two successive heats was of the order of 100 h. The computations were carried out on the Alabama Supercomputer Network's CRAY–C90 supercomputer, which is located in Huntsville, Alabama. Greater details on numerical methodology and other aspects of the computations has been reported by Lan [16].

4. Results and discussion

The computational results pertaining to the steady-state and transient flow field, heat transfer and phase change in the mold are presented in this section. As discussed above, two casting speeds of 1.27 and 2 cm/s were considered. The streamline patterns, temperature contours (isotherms), time-dependence of the size of the liquid, mushy and solid regions, casting surface tem-

perature signatures and heat flux variation along the mold are presented.

4.1. Steady-state flow and thermal fields

The streamline patterns and temperature contours within the mold for steady-state operating conditions for the two casting speeds of 1.27 and 2 cm/s are shown in Fig. 3(a) and (b), respectively. Due to the axisymmetric nature of the flow, only half of the mold region is selected for presentation. The streamlines (same as pathlines) which identify the paths traced by particles following the flow are presented on the left half of the figures, whereas the temperature contours are shown on the right half. The length of the mold was 0.6 m in these computations, so the mold extends from $z/R = 0$–5.91. In addition to the contour levels which clearly identify the solidus and liquidus temperatures (1470°C and 1500°C), the three different phases of the matter are highlighted using different shades in Fig. 3(a) and (b). The liquid zone ($T > 1500$°C) is highlighted with a dark shade, whereas the mushy zone (1470°C $< T <$ 1500°C) is identified with a grey shade. The thin solid shell of the casting ($T < 1470$°C) was not highlighted and is found on the far right side. For the low casting speed of 1.27 cm/s (Fig. 3(a)), the liquid pool penetrates to a depth of 5 mold radii, whereas for the high casting speed of 2 cm/s, this distance is of the order of 7 mold radii. The volumes of the liquid pools for the low and high casting speeds are 6.99×10^{-3} and 6.87×10^{-3} m^3, respectively. These zones correspond to 35.9% and 35.3% of the volume of the mold, respectively. The mushy zone extends farther down the mold and the volumes of the mushy regions within the computational domain for the low and high casting speeds are 3.89×10^{-2} and 5.07×10^{-2} m^3, respectively, which in turn correspond to 2 and 2.6 times the volume of the mold. The thickness of the solidified shell increases in the axial direction and at the bottom of the mold ($z/R = 5.91$), it is of the order of 13% and 6.2% of the mold radius for the low and high casting speeds, respectively.

For the two casting speeds considered the incoming jet of steel penetrates into the liquid pool. The liquid steel is then redirected into the mushy zone or floats up due to the buoyancy effect. The shearing at the jet boundary retards the fluid, which is then forced to float up due to the buoyancy force. On the other hand, the faster moving fluid in the core of the jet penetrates deeper in the liquid pool. Partly due to buoyant force effect and partly due to the resistance offered in the mushy zone ahead, the liquid is redirected sideways into the mushy region. Another feature of the flow in the liquid pool is the existence of a separated flow region neighboring the shear layer of the jet. The eye of this separated zone is located at $z/R = 1.5$–1.9 and $r/R = 0.3$–0.4 for the two casting speeds. With the Grashof numbers of the two cases being the same, the case of the low casting speed exhibits more dominance

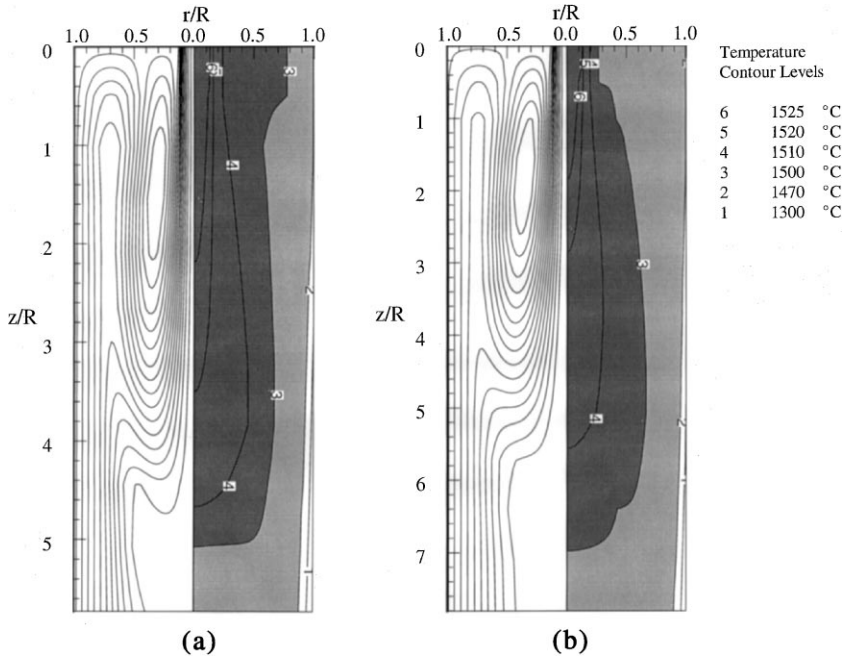

Fig. 3. Streamline patterns and temperature contours for steady-state operating conditions for the casting speed of (a) 1.27 cm/s and (b) 2 cm/s.

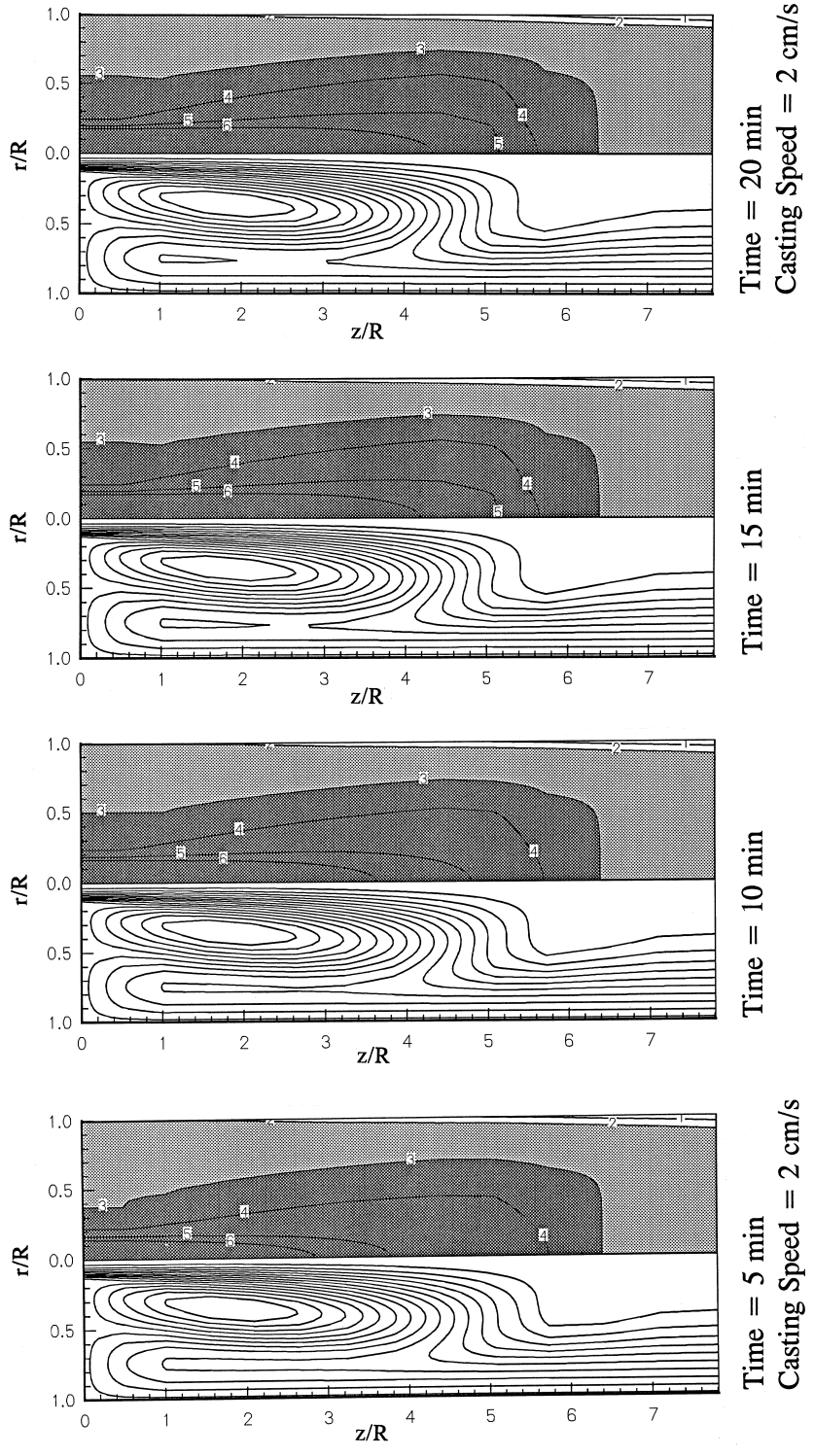

Fig. 4. Streamline patterns and temperature contours at different instants during the first cycle of the ladle change for the casting speed of 2 cm/s.

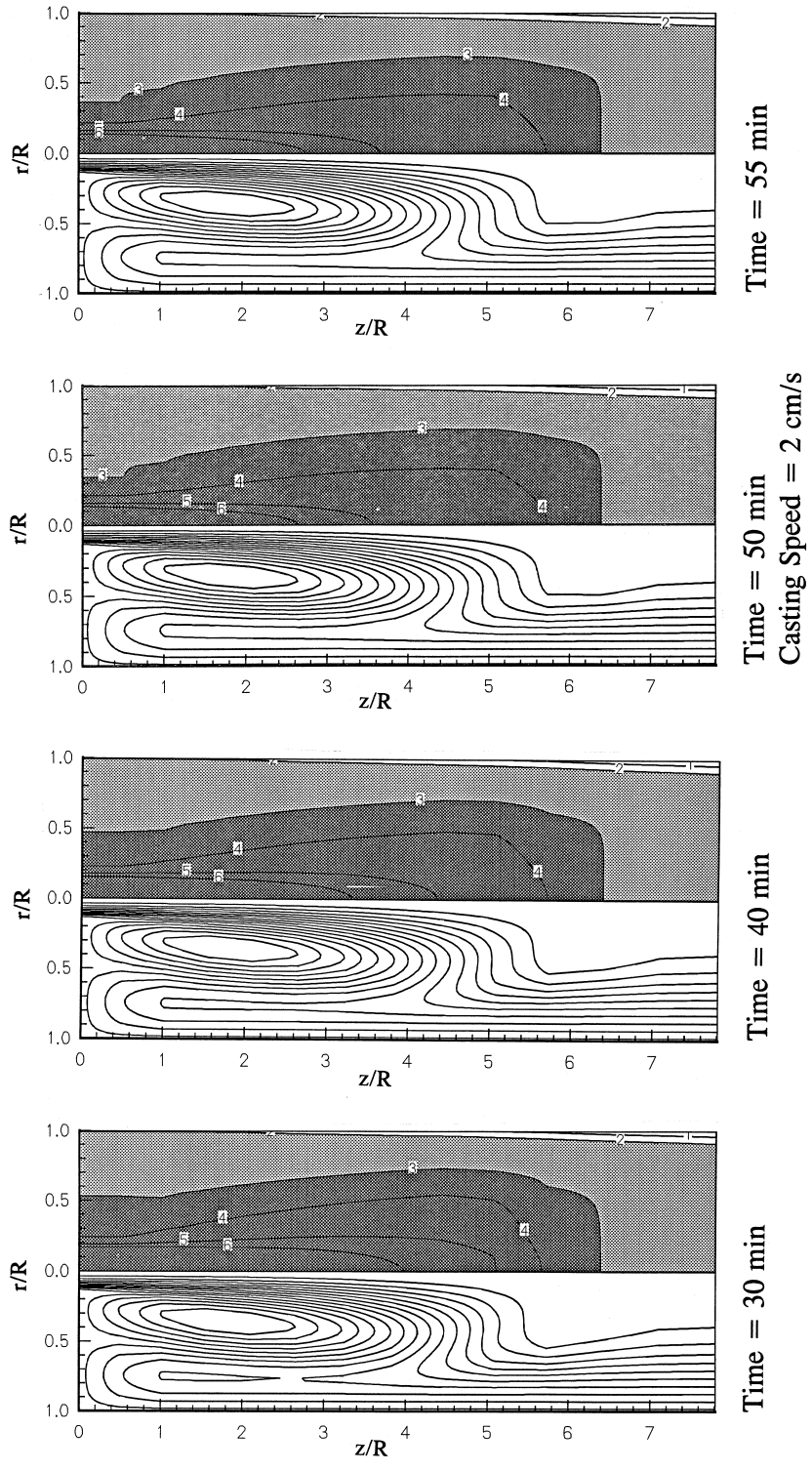

Fig. 4. (*continued*).

of the buoyancy effect, since its jet Reynolds number is smaller. This is clearly exhibited in Fig. 3(a) where the redirecting of the incoming jet takes place around 3.6 mold radii, whereas for the high casting speed this happens at about 4.6 mold radii (Fig. 3(b)).

5. Unsteady flow and thermal fields

The streamline patterns and temperature contours within the mold at different instants during the first cycle of the ladle change for the casting speed of 2 cm/s are shown in Fig. 4. The time instants selected for presentation are 5, 10, 15, 20, 30, 40, 50 and 55 min. Very similar results were obtained for the second cycle, thus those results are not repeated here. Due to the transient nature of the temperature of the incoming liquid steel (Fig. 2), the volume occupied by the liquid and mushy phases vary with time over a cycle. The volume occupied by the liquid phase expands (or bulges) in the radial direction toward the surface of the casting, whereas the axial extent of the liquid pool shrinks from 7 mold radii at $t = 0$ min to 6.4 mold radii at $t = 15$ min. This effect is reversed as the end of the first cycle is neared, at which time the liquid pool returns nearly to its original size. This phenomenon can be explained in the context of the relative importance of natural convection in comparison to forced convection. Under steady-state conditions for the casting speed of 2 cm/s, the ratio of $Gr/(Re_j)^2$ is 4.65, signifying that the effect of the buoyancy convection is of the same order of the forced convection. For the transient condition under study here, this ratio will increase by 28.3% at most over the cycle, suggesting that the buoyancy effect will become more significant as time passes, explaining the shrinking of the axial extent of the liquid pool and its radial growth. Similar findings were observed for the low casting speed of 1.27 cm/s and the detailed streamline patterns and temperature contours are not given here and can be found elsewhere [16].

Coordinates of the position of the solidified shell within the computational domain under steady-state conditions ($t = 0$) for the casting speeds of 1.27 and 2 cm/s are shown in Fig. 5(a) and (b), respectively. Due to intense cooling on the surface of the casting ($r/R = 1$), the thickness of the solidified shell increases in the axial direction and at the bottom of the mold ($z/R = 5.91$), the thickness of the shell is of the order of 13% and 6.2% of the mold radius for the low and high casting speeds, respectively. At the exit plane of the computational domain ($z/R = 25$), the thickness of the solidified shell is of the order of 52% and 34% of the mold radius for the low and high casting speeds, respectively. Inspection of the coordinates of the solidified shell under unsteady conditions showed that the variation of the shell thickness with time for both casting speeds followed the trend of the inlet jet temperature. Namely, as the inlet jet temperature increased at the beginning of the cycle, the shell thickness decreased, whereas once the inlet jet temperature was lowered in the second half of a given cycle, the shell thickness increased. Excessive thinning of

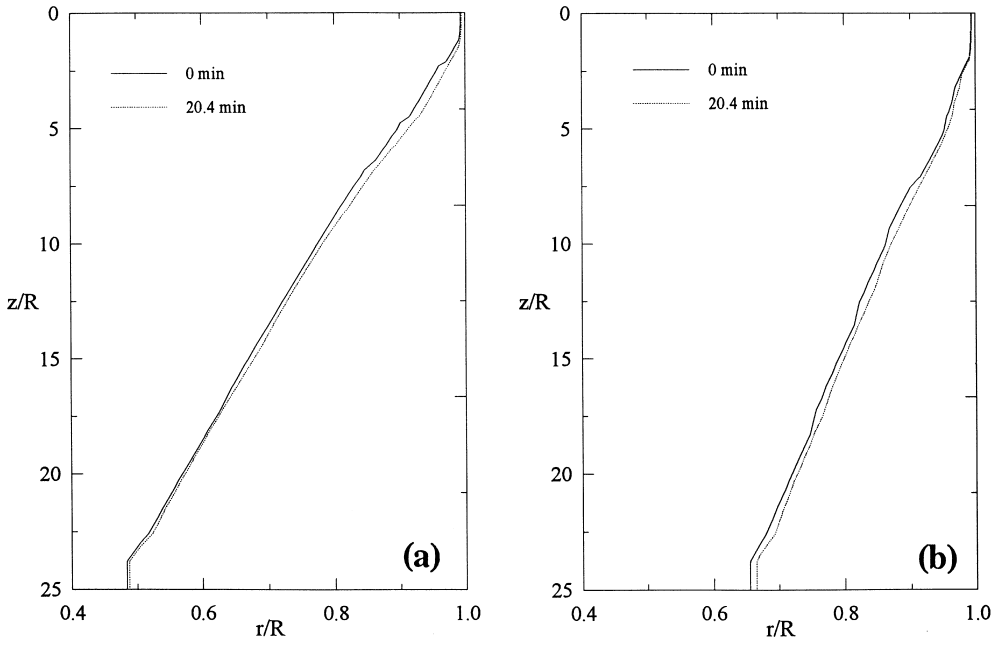

Fig. 5. Profiles of the solidified shell under steady-state condition ($t = 0$) and after 20.4 min for the casting speed of (a) 1.27 cm/s and (b) 2 cm/s.

the solidified shell can cause breakout. In the present study, the change of the solidified shell thickness within a cycle was found to be small, therefore the instantaneous profiles at different times are not provided. For the casting speed of 1.27 cm/s, the thinnest shell occurs after 20.4 min within the first cycle, as shown in Fig. 5(a). After 68.4 min within the second cycle, the shell thickness is very close to the one at 20.4 min, but a little thicker. With the casting speed of 2 cm/s, the corresponding time instants in each cycle were 20.4 and 70.4 min, respectively. Again, the thinnest shell thickness was observed at 20.4 min and is shown in Fig. 5(b).

The influence of the time-dependence of the inlet jet temperature on the temperature of the surface of the casting for the case of casting speed of 1.27 cm/s is shown in Fig. 6. Instantaneous casting surface temperature values are given at various axial stations within the mold ($z/R < 5.91$) and below the mold where the water sprays are located ($z/R > 5.91$). In general, the variation of the temperature of the surface of the casting with time followed the trends of the inlet temperature (Fig. 2). However, at certain axial locations ($2.65 \leqslant z/R \leqslant 4.45$), sharp temperature rise signatures are observed. These distinct temperature rise signatures are associated with axial stations where the radial thickness of the mushy zone is small (Fig. 3(a) and (b)) and the radial growth of the liquid pool with time promotes greater conduction transfer through the thinning mushy zone. The sharp surface temperature rise signatures associated with the high casting speed were found [16] to be more marked in comparison to those observed in Fig. 6.

Instantaneous local surface heat flux values ($q_w(z,t) = -\kappa(\partial T/\partial r)|_{r=R}$) at every axial station were also evaluated (Eqs. (6) and (7)). Since the value of the ambient temperature (T_a) is very small (30°C) compared to the temperature of the surface of the casting, the local surface heat flux values are nearly proportional to the surface temperature variations discussed here. The main distinction observed was a local increase of the local heat flux values at the bottom of the mold ($z/R = 5.91$) due to the switch to the spray cooling. The local heat flux values in the mold were integrated to determine the time-dependent spatially averaged or bulk mold heat flux, which provides information about the overall heat removed by the mold from the casting. The variation of the bulk heat flux ($q_b = \int_0^L q_w(z,t)\,dz/L$) with time is shown in Fig. 7(a), where it is non-dimensionalized with ($q_0 = \kappa(T_l - T_s)/R$). For both casting speeds, the heat removal rate by the mold vary over the two cycles of the ladle change operation indicating that extra cooling requirements must be taken into consideration in practical systems. Moreover, the demand for time-dependent cooling loads on the mold can be correlated to the abrupt surface temperature increases. The variation of the dimensionless volumes of the liquid and mushy zones with time is presented in Fig. 7(b). The instantaneous

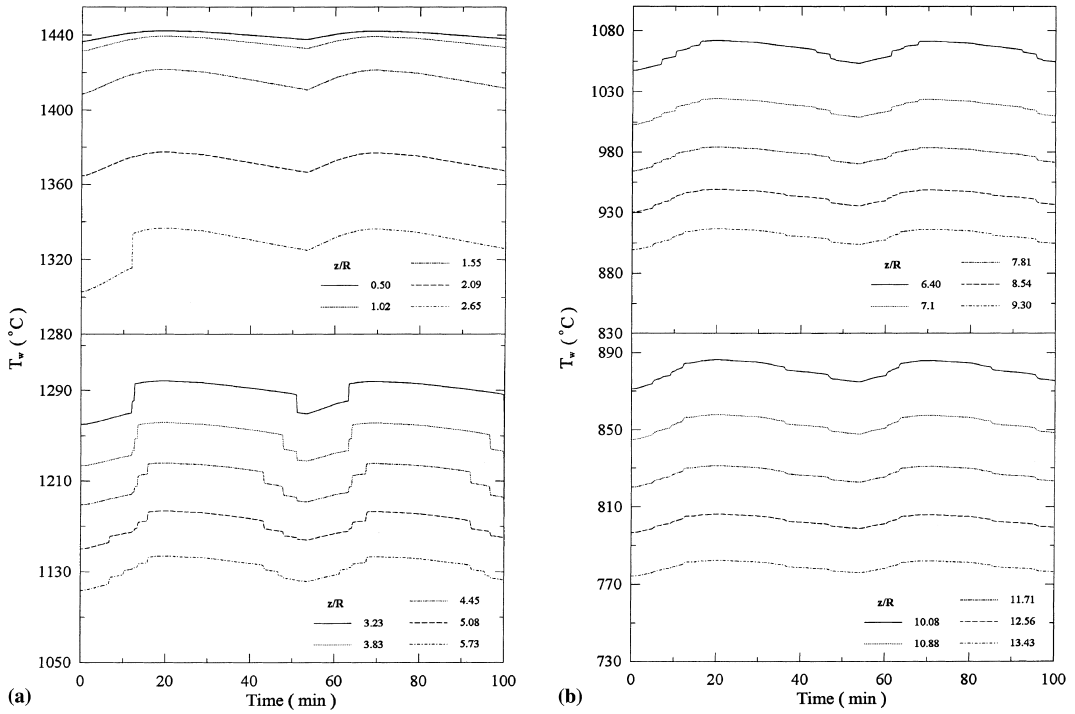

Fig. 6. Dependence of the temperature of the surface of the casting on time (casting speed of 1.27 cm/s).

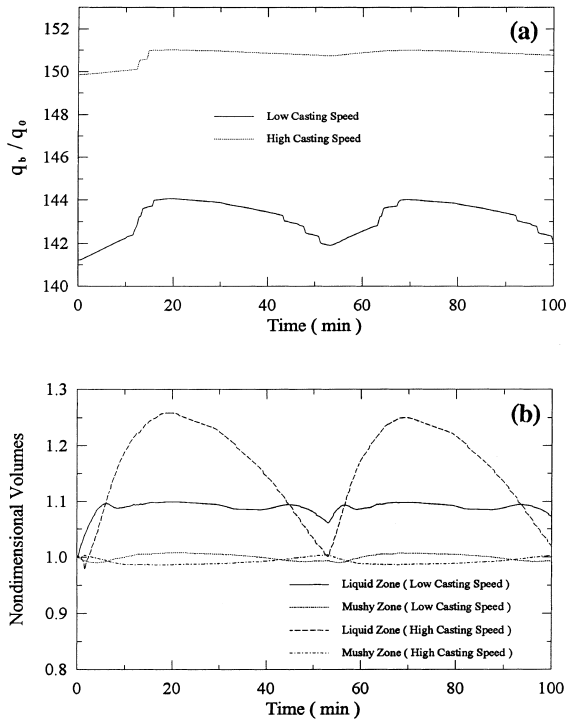

Fig. 7. Time dependence of (a) the bulk mold heat flux, and (b) the dimensionless volumes of the liquid and mushy zones.

volumes of the liquid and mushy zones are non-dimensionalized with their steady-state values mentioned earlier. For the low casting speed, the volume of the liquid pool increases almost linearly to about 109% of its initial size over time duration of 6 min. The volume of the liquid pool then remains fairly constant for the remainder of the ladle change operation while experiencing some shrinkage around 50 min (beginning of the second cycle). For the casting speed of 2 cm/s, the volume of the liquid pool increases to 125% of its initial size over time duration of 20 min. The volume of the liquid pool then decreases to its initial value at the beginning of the cycle and this behavior repeats itself during the second cycle. It is evident that the dependence of the liquid pool size on time for the high casting speed case is very similar to that of Fig. 2. The change of the size of the mushy zones over the period of two cycles for both casting speeds is very small (less than 2.5%) and it is noticed that there could be both gains and losses in size during the ladle change operation.

6. Conclusions

Based on the findings of the computational study presented in this paper, the following conclusions are drawn:

1. Due to the transient nature of the temperature of the incoming liquid steel during the ladle change operation, the volume occupied by the liquid and mushy phases varies over a cycle. The increase in size for the liquid pool depends on the casting speed and is as much as 25% when compared to the steady-state value. The size of the mushy zone does not vary greatly over the period of ladle change.
2. The volume occupied by the liquid phase generally expands in the radial direction toward the mold early during each cycle of the ladle change operation, whereas the axial extent of the liquid pool shrinks due to the greater influence of the buoyancy force. Later in the cycle, this trend is reversed as the inlet jet temperature is lowered.
3. The shrinkage of the thickness of the solidified shell during the ladle change operation is not noticeable for the conditions studied here, but it should be taken into consideration to avoid breakout.
4. Casting surface temperatures vary over the two cycles of the ladle change operation and distinct temperature rise signatures were detected. The bulk mold heat flux variation is also shown to vary with time in a cyclic fashion.

Acknowledgements

This research was supported by the CRAY Research, Inc., Eagan, MN through two University Research and Development Grant Program grants. The first author also acknowledges the financial support of the Advanced Manufacturing Technology Center and the Engineering Experiment Station at Auburn University. The opportunity of using the computer facilities/services of the Alabama Supercomputer Network is greatly appreciated.

References

[1] J. Szekely, R.T. Yadoya, The physical and mathematical modeling of the flow field in the mold region in continuous casting systems: Part I. Model studies with aqueous systems, Metall. Trans. 3 (1972) 2673–2680.
[2] J. Szekely, R.T. Yadoya, The physical and mathematical modeling of the flow field in the mold region in continuous casting systems. The mathematical representation of turbulent flow (Part II), Metall. Trans. 4 (1973) 1379–1388.
[3] J. Jezek, Flow visualization in continuous steel-casting, in: W. Merzkirch (Ed.), Flow Visualization II, Hemisphere, Washington, DC, 1982, pp. 173–177.
[4] J.M. Khodadadi, Y. Liang, F. Shen, Physical modeling of the turbulent flow in the mold of continuous casters using an aqueous system, AFS Trans. (1991) 421–428.
[5] W. Shyy, Y. Pang, G.B. Hunter, D.Y. Wei, M-.H. Chen, Modeling of turbulent transport and solidification during

continuous ingot casting, Int. J. Heat Mass Transfer 35 (5) (1992) 1229–1245.
[6] W. Shyy, Y. Pang, G.B. Hunter, D.Y. Wei, M-.H. Chen, Effect of turbulent heat transfer on continuous ingot solidification, Trans. ASME, J. Eng. Mater. Technol. 115 (1993) 8–16.
[7] M. Reza Aboutalebi, M. Hasan, R.I.L. Guthrie, Coupled turbulent flow, heat and solute transport in continuous casting processes, Metall. Mater. Trans. B 26 (4) (1995) 731–744.
[8] S. Chakraborty, Y. Sahai, Effect of varying ladle stream temperature on the melt flow and heat transfer in continuous casting tundishes, ISIJ Int. 31 (9) (1991) 960–967.
[9] S.V. Patankar, Numerical Heat Transfer and Fluid Flow, Hemisphere, Washington, DC, 1980.
[10] C.K.G. Lam, K. Bremhorst, A modified form of the k–ε model for predicting wall turbulence, Trans. ASME, J. Fluids Eng. 103 (1981) 456–460.
[11] V.C. Patel, W. Rodi, G. Scheuerer, Turbulence models for near-wall and low Reynolds number flows: a review, AIAA J. 23 (1985) 1308–1319.
[12] X.K. Lan, J.M. Khodadadi, F. Shen, Evaluation of six k–ε turbulence model predictions of flow in a continuous casting billet-mold water model using laser Doppler velocimetry measurements, Metall. Mater. Trans. B 28 (2) (1997) 321–332.
[13] V.R. Voller, C. Prakash, A fixed grid numerical modelling methodology for convection–diffusion mushy region phase-change problems, Int. J. Heat Mass Transfer 30 (8) (1987) 1709–1719.
[14] V.R. Voller, A.D. Brent, C. Prakash, Modelling the mushy region in a binary alloy, Appl. Math. Modell. 14 (1990) 320–326.
[15] The Iron and Steel Institute of Japan, Handbook of physico-chemical properties at high temperatures, Special Issue No. 41, ISIJ, Japan.
[16] X.K. Lan, Computational and experimental investigation of transport phenomena in a continuous casting mold, Ph.D. Thesis, Auburn University, Auburn, AL, 1996.